

Mixed-morphology supernova remnants: the case of SNR 0520–69.4 in the Large Magellanic Cloud

I. Ramírez-Ballinas¹,¹★ J. Reyes-Iturbide,² P. Ambrocio-Cruz³,³★ R. Gabbasov⁴,⁴ and M. Rosado¹,¹

¹*Instituto de Astronomía, Universidad Nacional Autónoma de México, Apdo. Postal 70-264, 04510 México City, México*

²*Tecnológico de Estudios Superiores de Tianguistenco, Carretera Tenango La Marquesa Km 22, Santiago Tianguistenco, Estado de México, México*

³*Escuela Superior de Tlahuelilpan, Universidad Autónoma del Estado de Hidalgo. Ex-Hacienda de San Servando. Col. Centro, CP 42780 Tlahuelilpan, Hgo. México*

⁴*Universidad Autónoma Metropolitana, Unidad Azcapotzalco, Av. San Pablo 180, Reynosa Tamaulipas, México City, México, 02200*

Accepted 2020 October 4. Received 2020 October 3; in original form 2020 June 19

ABSTRACT

We present observations in X-ray and optical emission of the supernova remnant (SNR) 0520–69.4 in the Large Magellanic Cloud. Using *XMM–Newton* observatory data, we produced images of the diffuse X-ray emission and spectra to obtain the X-ray parameters, such as luminosity and temperature, of hot plasma in the SNR. Diffuse X-ray emission with filled-centre morphology goes beyond the H α region, suggesting that the hot gas escapes through the pores of the H α shell. We fitted a model that has a plasma temperature of 1.1×10^7 K for an X-ray thermal luminosity of 3.3×10^{35} erg s^{−1}. However, from H α and [O III] Fabry–Perot observations obtained with the Marseille H α Survey of the Magellanic Clouds and the Milky Way at La Silla, European Southern Observatory, we are able to obtain physical parameters such as the velocity of the shock induced in the cloudlets emitting at optical wavelengths and the electron density of this gas. With the parameters described above, we test the model proposed by White & Long (1991, ApJ, 373, 543) for explaining the mixed-morphology observed.

Key words: ISM: individual objects: SNR 0520–69.4 – ISM: kinematics and dynamics – ISM: supernova remnants – Galaxies: Individual: Magellanic Clouds – X-rays: ISM.

1 INTRODUCTION

Supernovae (SNe) are the main source of energy in the interstellar medium (ISM), providing a kinetic energy $\sim 10^{51}$ erg. They play an important role in the chemical evolution of the Universe and are used (type Ia SNe) as standard candles in cosmology (Riess et al. 1998). Supernova remnants (SNRs) are the result of the interaction between the SN ejecta and the ISM. The forward shock associated with the SNR moves with velocities of $\sim 10^4$ km s^{−1} and heats the ISM to temperatures $\gtrsim 10^6$ K. Thus, the plasma emits in X-rays. However, a fraction of the initial kinetic energy accelerates cosmic-rays at the front shocks of SNRs (Koyama et al. 1995; Slane et al. 1999).

SNRs are an important tool to study SNe because they are observable for a few tens of thousands of years, while SNe are rare events lasting only several months (\sim two to three per century in a spiral galaxy). From the study of SNRs, we can infer the chemical composition of the hot (shocked) plasma, the degree of asymmetry present in the SN and the physical properties of the pre-shock ISM.

X-ray observations are a powerful tool to study SNRs (Maggi et al. 2016) and their progenitors, as X-ray spectroscopy of SNRs allows us to probe the abundances of the α and iron-group elements produced by the SNe. At the typical electron temperatures of SNR shocks (0.2–5 keV), all these elements have prominent emission lines in the 0.5–10 keV energy range, which are accessible to space observatories such as *XMM–Newton* and *Chandra*.

SNRs have been classified, based on their radio morphology: shell-like, Crab-like (Plerionic) and composite (shell-like SNRs containing Plerions). There is another group of SNRs with a peculiar morphology in radio and thermal X-ray emission: a centre-filled X-ray and shell-like radio morphology (Rho & Petre 1998). These emissions present slowly varying radial temperature and density profiles contrary to the standard Sedov model, and they are called mixed-morphology (MM) SNRs. There are models able to produce centrally enhanced X-ray emission. One of the main models considers that the SNR blastwave is moving in an inhomogeneous medium with denser cloudlets, which evaporate through the blastwave passage, increasing the gas density as well as the X-ray emission at the centre (White & Long 1991, hereafter WL). The solution proposed by WL incorporates a reasonable model of the conductive evaporation of cold clouds embedded in the hot gas behind the shock. The conduction is assumed to be saturated in the evaporative flows around the clouds, which is the case for most SNRs younger than $\sim 20\,000$ years old. In the present work, we test this model using SNR 0520–69.4 in the Large Magellanic Cloud (LMC), and for this a multiwavelength study is required.

The LMC is an excellent laboratory for multiwavelength studies of SNRs because of its small inclination angle and low internal extinction. The distance towards the LMC is relatively small (50 kpc; Pietrzyński et al. 2013). Interstellar absorption towards the LMC is much smaller ($N_{\text{H}} \lesssim 10^{21}$ cm^{−2}) than toward the Galactic Plane ($N_{\text{H}} \gtrsim 10^{22}$ cm^{−2}), which allows the detection of the soft X-ray emission. Furthermore, the LMC hosts a large sample of SNRs, all of them at the same distance of 50 kpc, on average. Finally, the LMC

* E-mail: I.Ramirez-Ballinas:iramirez@astro.unam.mx (IRB); silviap@uaeh.edu.mx (PAC)

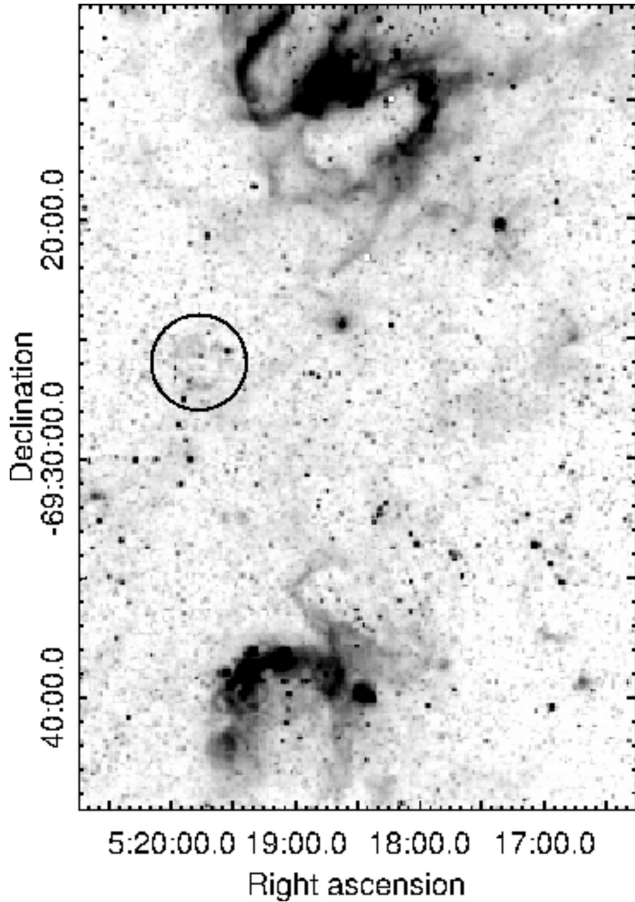


Figure 1. Optical image in $H\alpha$ of SNR 0520–69.4 (black circle) obtained with the MCELS (Smith et al. 2005). The objects LMC-N119 and LMC-N120 are located at the top and bottom of the figure, respectively.

has been studied in several bands of the electromagnetic spectrum. For these reasons, we decided to study SNR 0520–69.4 located in the LMC.

SNR 0520–69.4 has been extensively studied, from radio to X-ray wavelengths. From their optical observations, Mathewson et al. (1983) estimated a size of $138 \times 104 \text{ arcsec}^2$. Payne, White & Filipović (2008) found an enhanced $[S II]/H\alpha$ ratio of 0.8 typical for SNRs. In radio, with Australia Telescope Compact Array (ATCA) observations, it has been shown that this SNR exhibits a typical horseshoe morphology with $\alpha = -0.5$ and a radius $R = 26 \text{ pc}$. The radius is computed using a distance of 50 kpc to the LMC, but without evidence of polarization (which limits our understanding of the magnetic field structure in the post-shock region; Crawford, Filipovic & Payne 2008). In X-rays, a luminosity of $L_x = 6 \times 10^{35} \text{ erg s}^{-1}$ was reported (Mathewson et al. 1983). Also, identified as MCSNR J0519–6926 in their X-ray work, Maggi et al. (2016) have reported a luminosity of $L_x = 2.69 \times 10^{35} \text{ erg s}^{-1}$. The SNR 0520–69.4 is classified as an isolated SNR – that is, it does not belong to an OB association or H II region (Chu & Kennicutt 1988). It is located in the LMC, between the N119 and N120 complex H II regions (see the black circle in Fig. 1).

In this paper, we determine the hot gas physical parameters (i.e. density, temperature and luminosity) for SNR 0520–69.4 using *XMM-Newton* observations. From the optical data (using $H\alpha$ and $[O III]$ Fabry–Perot observations), we determine some other physical properties, such as the velocity of the shock induced in the dense

clouds responsible for the optical emission and its density, and the radial intensity distribution of the $H\alpha$ and $[O III]$ emission for this SNR. With these results, we can specify the evolutionary state of the SNR and so test the analytical and numerical WL models (Leahy & Williams 2017).

This paper is organized as follows. In Section 2, we describe the *XMM-Newton* observations and data reduction. The distribution of the X-ray-emitting gas is described in Section 3 and the analysis of its spectral properties is presented in Section 4. In Section 5, we present the optical observations and data reduction with the kinematic analysis, showing the results in Section 6. In Section 7, we describe the numerical model that uses a Python code (Leahy & Williams 2017). Finally, a discussion and conclusions are presented in Section 8.

2 XMM-NEWTON OBSERVATIONS AND DATA REDUCTION

The SNR 0520–69.4 was observed by *XMM-Newton* with the European Photon Imaging Camera (EPIC). The observations were performed on 2004 January 17 and correspond to the Obs.ID 0204770101 (PI: K. Borkowski). The EPIC-MOS and the EPIC-pn cameras were operated in the full frame mode. The three EPIC observations were obtained with the thin optical filter with a total observation time of 39.08 ks. The EPIC-pn, MOS1 and MOS2 cameras have exposure times of 30.43, 23.92 and 23.92 ks, respectively. The *XMM-Newton* pipeline products were processed using the *XMM-Newton* Science Analysis Software (SAS version 16.1) and the calibration files obtained on 2020 May 9.

We first analysed the observations making use of the *XMM* Extended Source Analysis Software (ESAS) tasks (Snowden, Collier & Kuntz 2004; Kuntz & Snowden 2008; Snowden et al. 2008) to produce images of SNR 0520–69.4 in different energy bands (see Section 3). This allowed us to identify the distribution of the diffuse X-ray emission and the locations of point-like sources. We created three EPIC images in the 0.3–1.0, 1.0–2.0 and 2.0–7.0 keV energy ranges, which are labelled as soft, medium and hard bands, respectively. Following the ESAS cookbook, individual pn, MOS1 and MOS2 images were created, merged and, finally, corrected by their exposure maps. The resultant exposure-map-corrected, background-subtracted EPIC (pn+MOS1+MOS2) image of the soft X-ray emission and a colour-composite image combining the three bands are shown in Fig. 2. Each band image has been adaptively smoothed using the ESAS task `adapt` requesting 20 counts under the smoothing kernel for the soft and medium bands and 10 counts for the hard band.

Whereas the *XMM* ESAS tasks apply very restrictive event selection criteria, which are appropriate for the analysis of the spatial distribution of the X-ray emission, these are not required for spectral analysis, because the final net exposure times are short: 8.1, 11.3 and 11.6 ks for the pn, MOS1 and MOS2 cameras, respectively. The method used for spectral analysis is described in Section 4.

3 DISTRIBUTION OF THE X-RAY EMITTING GAS IN SNR 0520–69.4

Fig. 2 shows the X-ray emission from SNR 0520–69.4. This SNR is located at the centre of the visual field. The image also shows several point sources unrelated to the SNR. The emission occurs mainly in the soft (0.3–1.0 keV) and intermediate (1.0–2.0 keV) band energy. There is no detected emission in the hard X-ray band (2.0–7.0 keV). We extracted the brightness distribution profiles along horizontal and vertical apertures that cross the centre of the SNR (see Fig. 3).

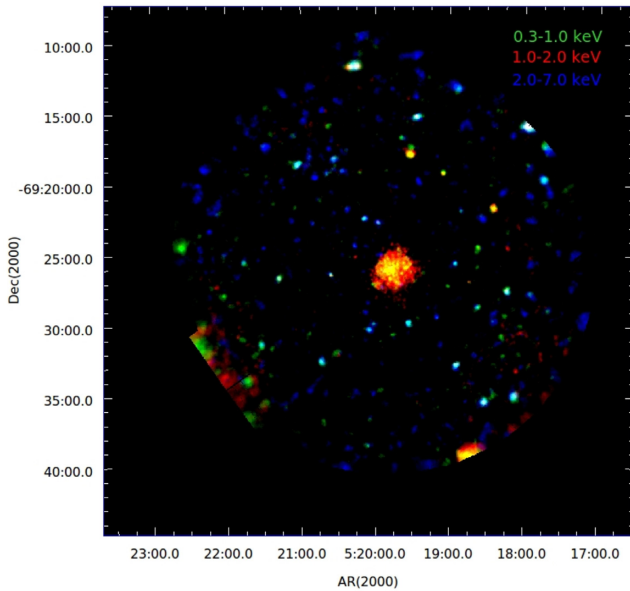


Figure 2. *XMM-Newton* EPIC exposure and background-corrected images of the X-ray emission from SNR 0520–69.4 located at the centre of the field of vision. Green, red and blue colours correspond to energy ranges 0.3–1.0, 1.0–2.0 and 2.0–7.0 keV, respectively.

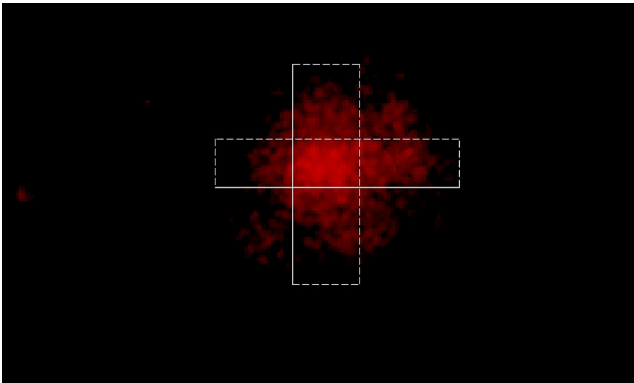


Figure 3. Overlapping apertures used to extract the brightness distribution profile from the *XMM-Newton* EPIC image (Fig. 2).

The profiles are shown in Fig. 4, where the top and bottom panels correspond to the horizontal and vertical cuts, respectively. These show that the brightness is maximum at the centre of the SNR, decreasing with the distance from the centre.

In order to analyse the spatial distribution of the soft X-ray emission of SNR 0520–69.4, we show a comparison between the X-ray emission and the $H\alpha$ emission taken from the Magellanic Cloud Emission Line Survey (MCELS). The top panel of Fig. 5 shows a composite image with $H\alpha$ (red) and soft X-ray (blue) emission. The X-ray emission extends beyond the optical shell. This is because of the incomplete confinement of the hot gas by the shell emitting $H\alpha$. This hot gas leakage through low-density pores in the shell can be observed in the bottom panel of Fig. 5, where we also superpose on the $H\alpha$ emission the X-ray contours at 3σ , 5σ and 7σ above the background, taken from Fig. 2. We note that there are three regions or pores in the shell where hot gas escapes, located towards the north, south-east and south-west.

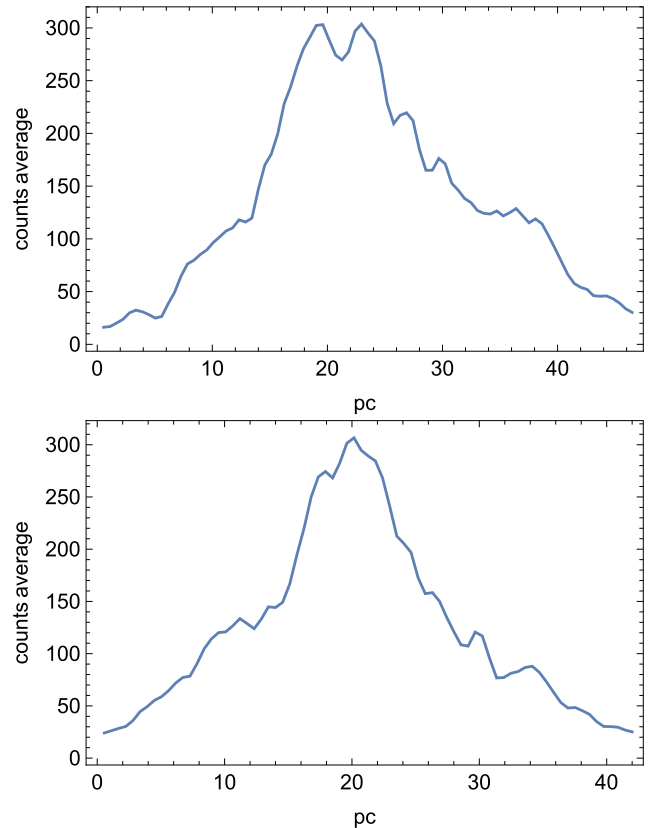


Figure 4. Brightness profiles extracted from the *XMM-Newton* image of SNR 0520–69.4 (see Fig. 3): top, horizontal cut; bottom, vertical cut.

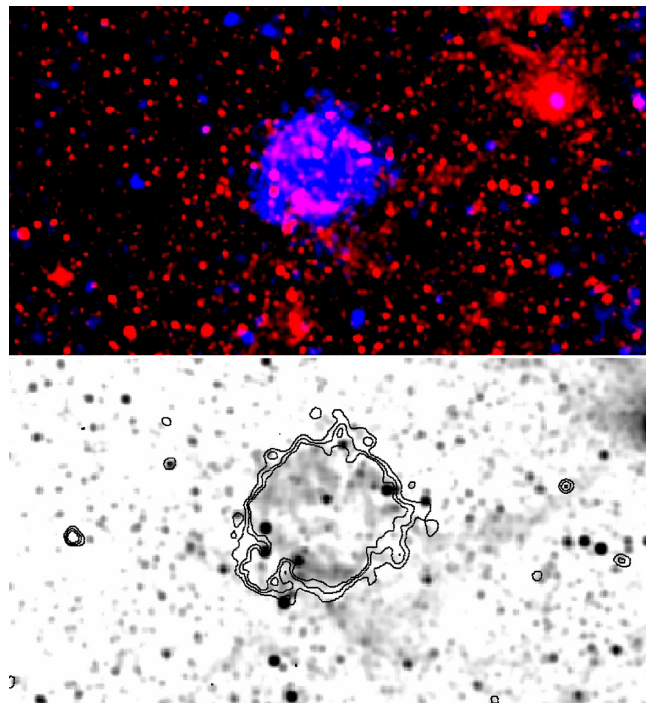


Figure 5. Colour-composite images of SNR 0520–69.4. The top panel shows the optical and X-ray composition. Red and blue colours correspond to $H\alpha$ and the soft X-ray band, respectively. The bottom panel shows an image in $H\alpha$ taken from the MCELS (in grey). Superposed on to this image are some of the X-ray contours at levels of 3σ , 5σ and 7σ , taken from Fig. 2.

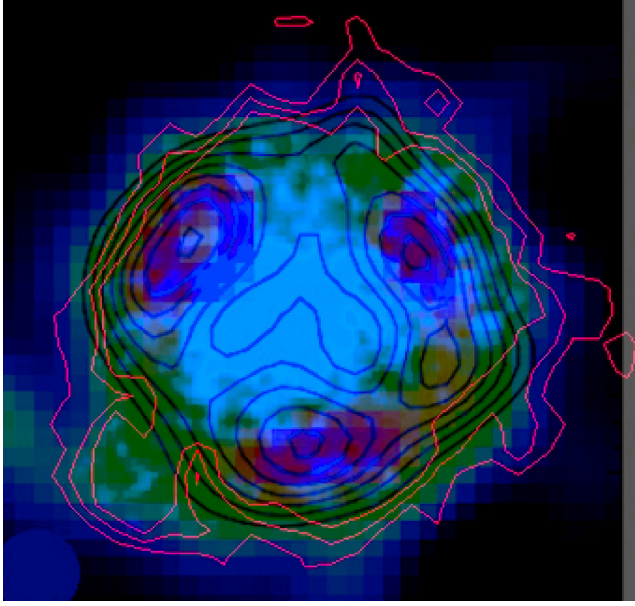


Figure 6. Composite image, with superposed contour X-ray radiation (red), and image of the radio emission (purple, blue and green, taken from ATCA; Crawford et al. 2008). Note the X-ray protrusions are to the north (up) and to the west (right).

To analyse the spatial correlation between the X-ray and radio emission, in Fig. 6 we produce an image (taken from Crawford et al. 2008) that shows an overlay from contours in X-ray emission (red) with contours in radio (black). We observe a spatial correlation between both emissions, although the X-ray emission is slightly more extended than in radio because of the hot gas leakage described above. So, we can conclude that radio emitting gas encloses the X-

ray emitting gas, meaning that SNR 0520–69.4 can be classified as an MM SNR (Rho & Petre 1996).

4 ANALYSIS OF X-RAY SPECTRAL PROPERTIES

The observation data files were processed using the SAS tasks *eproc* and *emproc* to produce the corresponding event files. The spectra were extracted using the task *evselect*, both for the SNR region and for the background. Circular apertures with angular radii of 1.5 and 1.2 arcmin, respectively, were extracted for these regions (equivalent to 21.8 and 17.5 pc) free of point source contamination; the associated calibration matrices were obtained with the tasks *arfgen* and *rmfgen*. The background-subtracted spectra from the pn, MOS1 and MOS2 cameras are shown in Fig. 7.

The EPIC spectra of SNR 0520–69.4 are shown in Fig. 7. To perform the spectral analysis, the software *xspec* (version 12.9; Arnaud 1996) was used. Following previous studies of the extended X-ray emission from SNRs in the LMC, we have modelled the X-ray spectra using the absorbed *vpshock* plane-parallel shock plasma model at constant temperature with the *tbabs* absorption model (Wilms, Allen & McCray 2000). The abundances were set similar to the ISM values of the LMC (Maggi et al. 2016; see Table 1).

The resultant model spectra were compared with the observed X-ray spectra in the [0.3–2.0] keV energy range, where χ^2 statistics are used to evaluate the goodness of the fits. A minimum of 30 counts per bin was requested for the spectral fits. The best-fitting model is superposed to the background-subtracted EPIC spectra in Fig. 7.

According to this figure, the most prominent lines are those of the O VII at 0.58 and O VIII at 0.65 keV, although the former is brighter in these spectra. The effective exposure time for the pn, MOS1 and MOS2, are 20 220, 22 990 and 23 080 s respectively. The resultant count rate for the pn is 0.54 counts s^{−1}, and for the MOS1 and MOS2

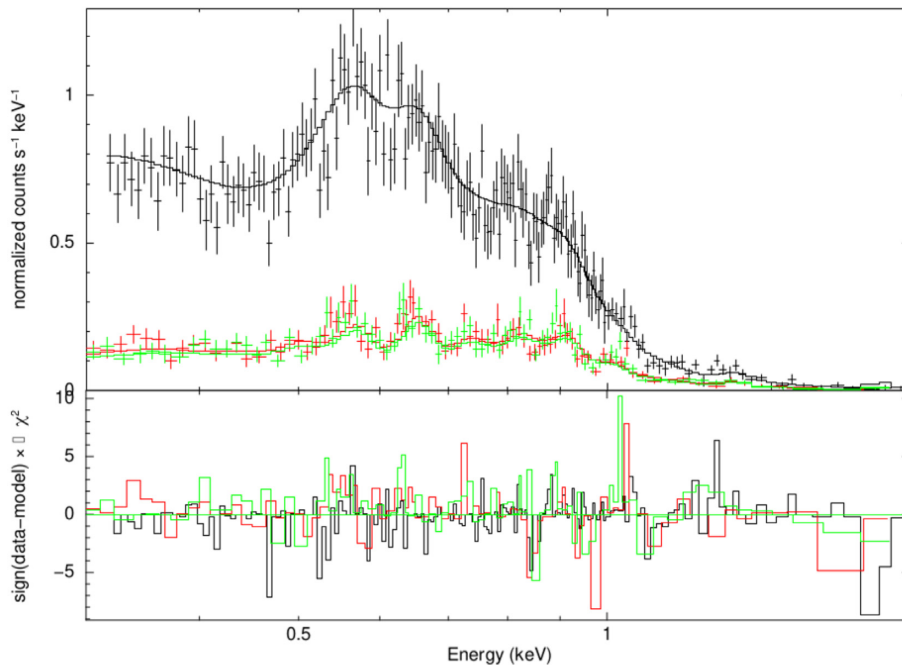


Figure 7. Background-subtracted *XMM-Newton* EPIC spectra of SNR 0520–69.4. The solid lines show the best-fitting model. Different colours represent extracted spectra from different cameras. Black, red and green are EPIC-pn, EPIC-MOS1 and EPIC-MOS2, respectively. Residuals are shown in the bottom panel.

Table 1. LMC abundances used for the spectral fit (Maggi et al. 2016).

Element	X/X_{\odot}
C	0.20
N	0.47
O	0.21
Ne	0.28
Mg	0.33
Si	0.69
S	0.36
Fe	0.35

Table 2. Physical parameters obtained for SNR 0520–69.4.

V_s	600 km s^{-1}
N_H	$1.0 \times 10^{20} \text{ cm}^{-2}$
kT_1	$(1.0 \pm 0.08) \text{ keV}$
A_1	$2.53 \times 10^{-4} \text{ cm}^{-5}$
EM	$8.85 \times 10^{57} \text{ cm}^{-3}$
f_x	$(1.10 \pm 0.01) \times 10^{-12} \text{ erg cm}^{-2} \text{ s}^{-1}$
L_x	$(3.3 \pm 0.2) \times 10^{35} \text{ erg s}^{-1}$
$n_{e,x}$	0.13 cm^{-3}
τ	$(3.6 \pm 0.3) \times 10^{10} \text{ s cm}^{-3}$
t_{ion}	$(8.8 \pm 0.8) \text{ kyr}$
t_{rem}	$\sim 17\,000 \text{ yr}$
P_x	$2.29 \times 10^{-10} \text{ dyn cm}^{-2}$
E_0	$4.87 \times 10^{50} \text{ erg}$

spectra $0.14 \text{ counts s}^{-1}$, which corresponds to a total of 10 823, 3218 and 3231 counts, respectively.

We used a single absorbing column density, $N_H = 1.0 \times 10^{20} \text{ cm}^{-2}$, which is of the order of the measures of column densities of the LMC, average $N_H = 6.4 \times 10^{20} \text{ cm}^{-2}$ (Dickey & Lockman 1990). The best-fitting model gave a reduced $\chi^2 = 1.55$. The best-fitting parameters in the $[0.3\text{--}2.0] \text{ keV}$ energy band are listed in Table 2. The observed total flux of the diffuse X-ray emission, corrected by absorption, was determined at the LMC distance. The electron density $n_{e,x}$ was obtained by assuming a spherical morphology. The emission measure (EM) can be determined by an analysis of X-ray spectrum observations of an SNR, and is given by the norm parameter from fitting the X-ray spectrum:

$$A = \frac{10^{-14}}{4\pi D^2} EM. \quad (1)$$

Here, D is the distance to the SNR and A is the normalization parameter. Table 2 also lists the following parameters: luminosity L , given by $L = 4\pi D^2 f_x$, where f_x is the dereddened X-ray flux; the ionization time-scale τ given by $\tau = n_{e,x} t_{\text{ion}}$; the shock velocity V_s given by

$$V_s = \left(\frac{16k}{3\mu} T \right)^{1/2}, \quad (2)$$

where kT corresponds to plasma temperature and $\mu = (14/11)m_H$ (Weaver et al. 1977); the age of the remnant t_{rem} , which can be obtained by $V_s = \frac{2}{5} R/t_{\text{rem}}$. Pressure is given by

$$P_x = n_{e,x} kT \quad (3)$$

and, finally, the initial energy E_0 of the SN is

$$E_0 = \frac{25}{3(2.02)} P_x R_x^3 \quad (4)$$

(Cox & Anderson 1982).

Table 3. Scanning FP interferometer main parameters and observations.

FP parameter/observation	H α	[O III]
Lambda (\AA)	6563	5007
Interference order (p) at H α	796	2609
Effective finesse (F)	12.5	12.5
Scanning steps ^a	24	40
Spectral sampling (km s^{-1})	16	3
Spectral resolution (R)	10 000	32 000
Sampling spectral resolution (km s^{-1})	16 ± 3	3 ± 2
Free spectral range (\AA)	8.27	1.9
Free spectral range (km s^{-1})	337	115
Field of view (FOV, arcmin)	38	38
Spatial resolution (arcsec pixel ⁻¹)	9×9	9×9
Exposure time for FOV (h)	2	2.22
Total exposure time (s)	7200	8000

^a Following Shannon–Nyquist criteria (Shannon 1949).

5 OPTICAL OBSERVATIONS AND DATA REDUCTION

The optical observations were carried out in the framework of the H α survey of the Magellanic Clouds and the Milky Way, made with a 36-cm diameter telescope (located at La Silla, ESO) on 1993 February 26 and 27. The observations of SNR 0520–69.4 were carried out with a scanning Fabry–Perot (FP) interferometer attached to the Cassegrain focus of the 36-cm telescope and operated under the same conditions as during the observations of the H II region N119 described in Ambrocio-Cruz et al. (2008), because this SNR falls in the same data cube asat N119, at both H α and [O III] $\lambda 5007 \text{ \AA}$. The field of view is $38 \times 38 \text{ arcmin}^2$, covered by the (256×256) pixels of the photon counter camera, which gives a spatial resolution of 9 arcsec per pixel. We have obtained FP data cubes at H α and [O III] $\lambda 5007 \text{ \AA}$. The calibration data cubes were taken before and after the nebular exposures in order to check for possible flexures of the equipment. The nebular data cubes have total exposure times of 7200 and 8000 s for H α and [O III] $\lambda 5007 \text{ \AA}$, respectively. Table 3 lists the main parameters of the survey H α and [O III] FP interferometer and of the observations of SNR 0520–69.4.

Data reduction was carried out by means of the specialized software CIGALE (Le Coarer et al. 1993), which was designed specifically for the acquisition and reduction of data obtained with a scanning Fabry–Perot interferometer. The software allows us to do the flat-field correction, wavelength calibration, construction of velocity maps, and radial velocity profile extraction and fitting. Using this software, we have also been able to integrate the line emission and separately construct monochromatic and continuum images from the Fabry–Perot data cubes. A complete description of the instrumentation, including data acquisition and reduction techniques, is given in Amram et al. (1991) and Le Coarer et al. (1992).

6 RESULTS FOR SNR 0520–69.4

6.1 Optical results

6.1.1 H α and [O III] Fabry–Perot kinematics of the SNR

We use both the H α and [O III] data cubes. Once calibrated in wavelength, we inspect the morphologies of the SNR emission at different velocities and in the different emission lines. According to radiative shock models, the detection of emission in the [O III] line of

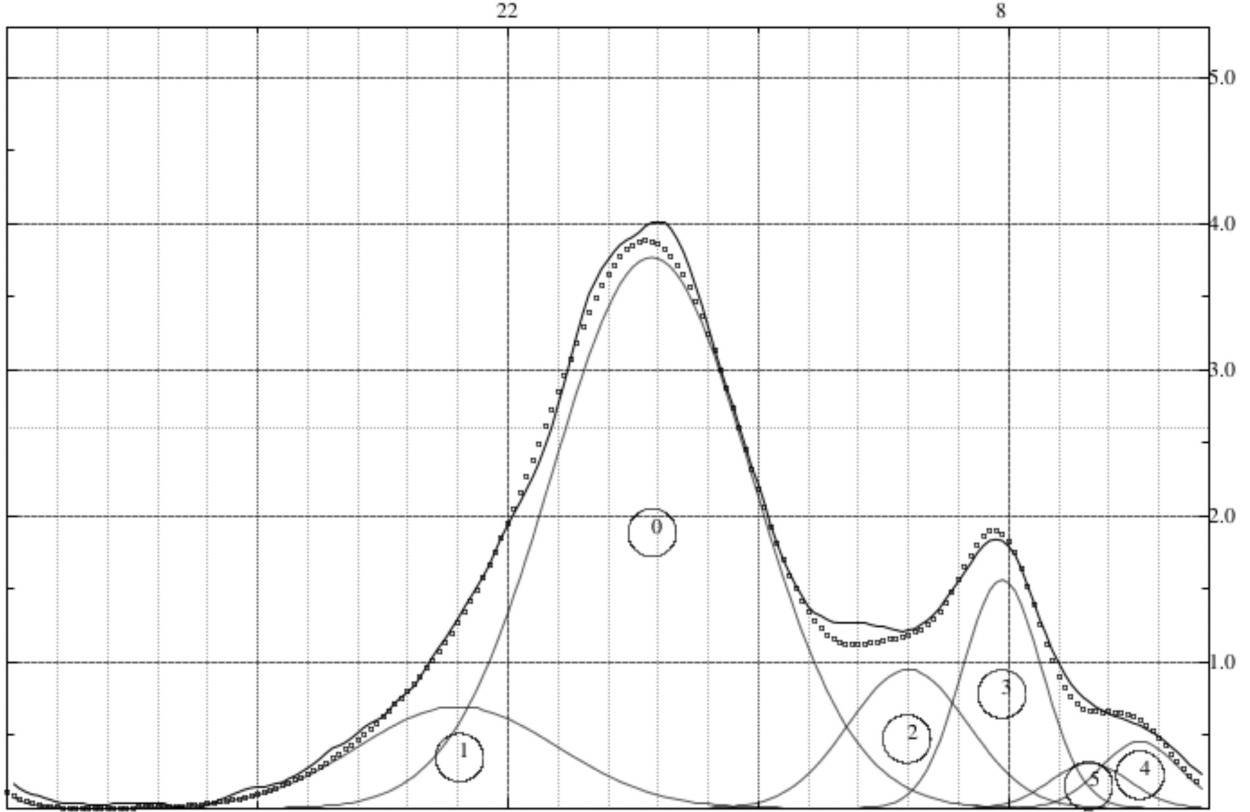


Figure 8. Integrated radial velocity profile of the whole $H\alpha$ emission of SNR 0520–69.4 obtained from the $H\alpha$ survey of the LMC Fabry–Perot observations (Ambrocio-Cruz et al. 2016). The intensity scale is in arbitrary units, the x direction corresponds to the 24 channels of the radial velocity cube or lambda cube, with each channel separated by 15.7 km s^{-1} , and the 0 channel corresponds to $V_{\text{hel}} = 250 \text{ km s}^{-1}$. Several Gaussian radial velocity components are present (marked by the encircled numbers). The dotted line includes the contribution of all the Gaussian components and it was fitted to the observed velocity profile (solid line). Radial velocities span from $V_{\text{hel}} = 204 \text{ km s}^{-1}$ (component 1) to $V_{\text{hel}} = 401 \text{ km s}^{-1}$ (component 4). Components 3 and 5 are probably sky-lines.

the SNR implies that the shock should have velocities approaching 100 km s^{-1} . However, this emission is weaker than the corresponding $H\alpha$ emission (see the right panel of Figure 8) and, consequently, in this work we are measuring the kinematics from the $H\alpha$ velocity cube because of its higher S/N. From the $H\alpha$ velocity cube, we extracted radial velocity profiles integrated over several regions of interest. The extracted velocity profiles were analysed with the software CIGALE, which allows us to fit one or more Gaussian functions once the deconvolution of each component with the FP instrumental function (an Airy Function) is achieved. Fig. 8 shows one of those integrated radial velocity profiles. As one can see, the velocity profile is broad (with a width of more than 200 km s^{-1}), implying that complex internal motions are present. In this paper, we quote the radial velocity values corrected from the Earth’s rotation and revolution around the Sun, called heliocentric velocities (V_{hel}). We are able to find a bright velocity component (the main component) at $V_{\text{hel}} = 264 \text{ km s}^{-1}$ – and a full width at half-maximum (FWHM) = 75 km s^{-1} – corresponding to the systemic velocity of the remnant and two high-velocity wings (fainter but with large S/N) with $V_{\text{hel}} = 204 \text{ km s}^{-1}$ and $V_{\text{hel}} = 374 \text{ km s}^{-1}$ (FWHM = 75 km s^{-1}). Thus, the SNR ionized gas has velocities spanning at least 170 km s^{-1} and the velocity components identified by our kinematics imply an expansion velocity, $V_{\text{exp}} \gtrsim 85 \text{ km s}^{-1}$. This expansion velocity will be adopted as the secondary shock velocity induced in dense clumps immersed in a rarefied medium, where the main shock expansion takes place, according to the model of McKee & Cowie (1975).

6.1.2 Derivation of other important parameters of SNR 0520–69.4

Our Fabry–Perot imaging observations allow us to measure the angular diameter of SNR 0520–69.4. At $H\alpha$, the angular radius is 1.5 arcmin , corresponding to a linear radius of 22 pc for a distance of 50 kpc to the LMC. From our [O III] data cube, we have measured a radius of 1.8 arcmin for the SNR [O III] emission corresponding to a linear radius of 26 pc . In Section 8, we discuss the origin of this discrepancy, which also occurs for the X-ray emission. We have obtained cuts along the major axis of the [O III] and $H\alpha$ images of the SNR. These brightness profiles are also shown in Fig. 9 (lower panel). Contrary to the filled-centre X-ray brightness profile shown in Fig. 4, the brightness profiles of optical emission lines do not show maximum intensity at the centre; they appear limb-brightened. Thus, in this particular case, the optical line emission appears to follow the properties of the radio emission. To obtain the other SNR properties from optical data, we adopt $R = 26 \text{ pc}$.

From the interferometric observations, we can also estimate another important physical parameter, the $H\alpha$ surface brightness $S(H\alpha)$, from which we can then compute the SNR density of the dense cloudlets. The intrinsic flux is related to the parameters used for the line fitting (i.e. the height of the Gaussian function, the FWHM and the area occupied by the nebula). To convert our measures to units of flux, we used the relation obtained by Ambrocio-Cruz (1999) that gives $1 \text{ count} \times \text{channel}/(\text{pixel} \times \text{hour}) = 1.84 \text{ Rayleigh}$ with $1 \text{ Rayleigh} = 2.4 \times 10^{-7} \text{ erg cm}^{-2} \text{ s}^{-1} \text{ sr}^{-1}$. We obtained $S(H\alpha) = 1.8 \times 10^{-5} \text{ erg cm}^{-2} \text{ s}^{-1} \text{ sr}^{-1}$. We do not correct the

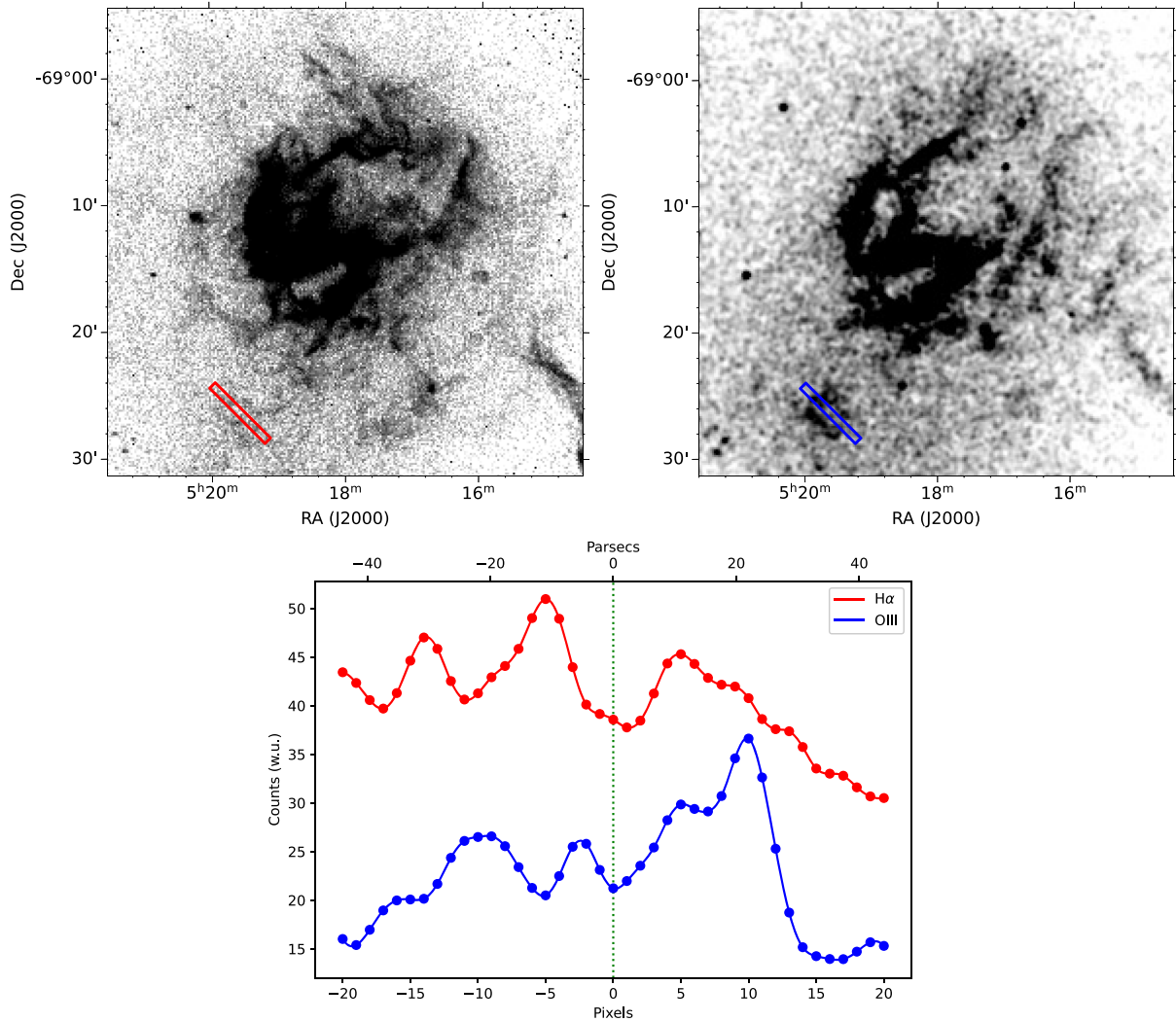


Figure 9. Left panel: $H\alpha$ monochromatic image of the 39×39 arcmin² field where the SNR is detected to the south-east of the image. Right panel: $[O\text{ III}]$ image of the same field as in the $H\alpha$ image. Lower panel: $H\alpha$ (red) and $[O\text{ III}]$ (blue) surface brightness cuts averaged over a box 4 pixels wide and 40 pixels long (shown by red and blue boxes in the images). The profiles are given in working units and extracted along the major axis of the SNR going from south-west to north-east. The centre of the SNR is marked as a dotted vertical line.

obtained $H\alpha$ surface brightness from reddening as in this field (see the Ambrocio-Cruz et al. 2008 study of the N119 region) the reddening is negligible, $E(B - V) = 0.15$ mag. Having obtained the surface brightness values, we can derive the rms electron density ($\langle n \rangle_{\text{rms}}$ in units of cm⁻³; Osterbrock 1989): These parameters are related via (Osterbrock 1989)

$$\langle n \rangle_{\text{rms}} = [S(H\alpha)/17.5 \times 10^{-8} R]^{1/2},$$

where R is the radius of the nebula in pc. With these values, we obtain $\langle n \rangle_{\text{rms}} = 2.0\text{--}2.6$ cm⁻³. The pressure of the optical emitting gas $P = \langle n \rangle_{\text{rms}} kT$ is thus 4.60×10^{-12} dyn cm⁻², assuming a temperature of the optical emitting gas of 10 000 K. In addition, the $H\alpha$ luminosity is $L(H\alpha) = 1.45 \times 10^{36}$ erg s⁻¹.

7 NUMERICAL SIMULATIONS AND RESULTS

In order to reproduce the physical conditions that determine aspects of SNR evolution such as shock radius and velocity in a more realistic model, which include ejecta and circumstellar medium (CSM) density profiles, we used a Python code described by Leahy &

Williams (2017). This software package allows the inclusion of constraints from observations to obtain SNR physical properties of interest following the WL treatment, which developed self-similar models for SNR evolution in a cloudy ISM. WL models depend on two parameters: a cloud density parameter $C = \rho_c/\rho_o$, where ρ_c and ρ_o are the cloud and the intercloud densities, and an evaporation time-scale parameter $\tau^* = t_{\text{evap}}/t$, with t_{evap} and t being the evaporation time-scale and the age of the SNR, respectively. WL models reduce to one parameter C/τ^* in the limit as $C \rightarrow \infty$ and $\tau^* \rightarrow \infty$ simultaneously. The WL self-similar models become the standard self-similar Sedov–Taylor model for the evolution of the blast wave radius when $C \ll 1$ or $\tau^* \gg C$ (WL).

For the case of highly saturated heat flux, which is a typical condition in SNRs during the non-radiative phase, the evaporation time-scale is

$$t_{\text{evap}} = 1.48 \times 10^3 \frac{R_{\text{cl}}^{7/6} n_{\text{cl}}}{P_x^{5/6}} \text{Myr}, \quad (5)$$

where R_{cl} is the cloud radius, n_{cl} is the cloud density and P_x is the thermal pressure of the hot gas, which is assumed to be roughly

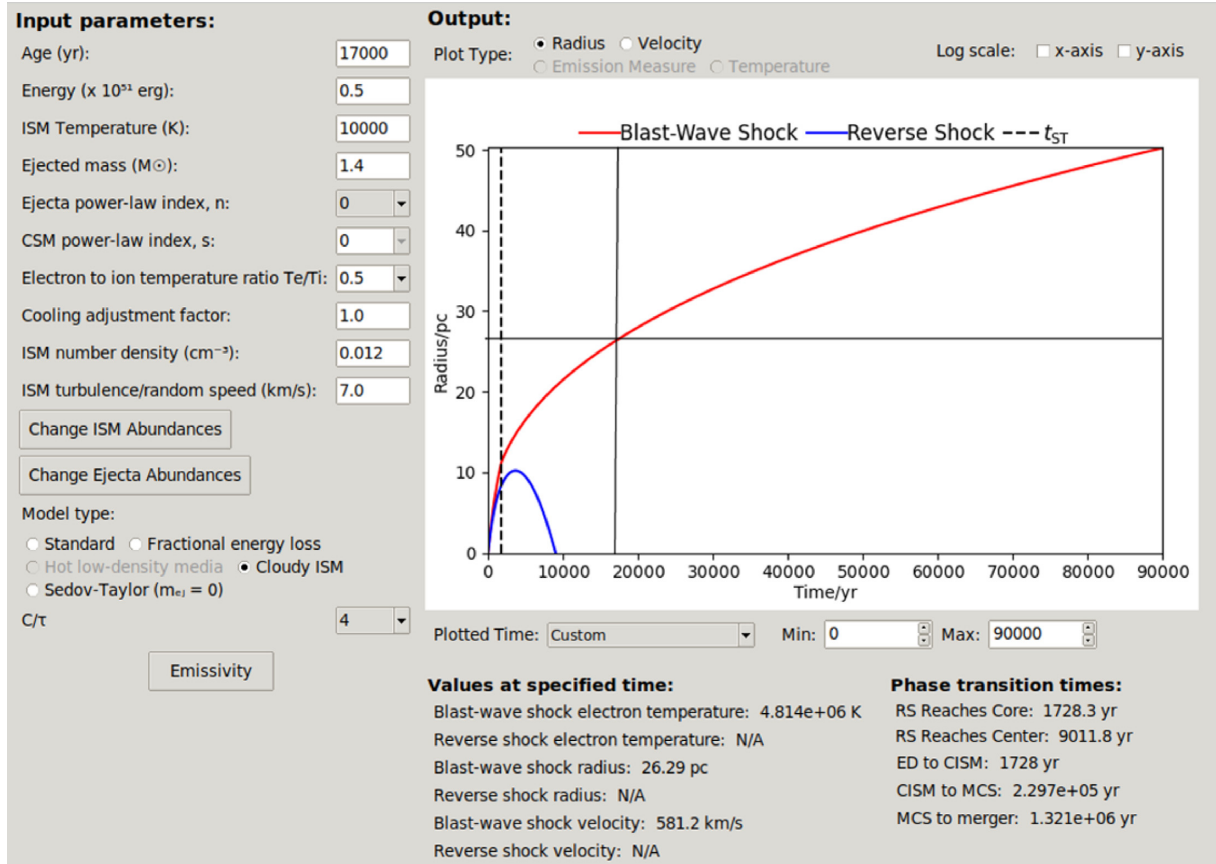


Figure 10. Screenshot of the main screen of the SNR modelling program. The boxes at the left side represent the input parameters. Top right: selection of the output plot of radius versus time; this plot represents the size of blast-wave shock (red) and of reverse shock (blue). Bottom right: output values at the specified time and the phase transition times. The vertical continuous line denotes the SNR age and the horizontal continuous line denotes respective radius.

Table 4. Physical parameters of SNR 0520–69.4, derived from this work, used in the models from WL.

V_s	600 km s^{-1}
t_{rem}	17 000 yr
n_{cl}	$2.0\text{--}2.6 \text{ cm}^{-3}$
R_{cl}	1.0 pc
t_{evap}	19 000 yr
τ^*	~ 2.0
C	15.0–20.0
$\langle T \rangle$	2.3×10^6 K
C/τ^*	7.7–10

equal to pressure in the cloud. The CSM density can be described by a power law $\rho_{\text{CSM}} = \rho_s r^{-s}$. Here, we assume a constant density medium, $s = 0$. The unshocked ejecta is taken to have a power-law density profile $\rho_{\text{ej}} \propto r^{-n}$.

To evaluate the case of SNR 0520–69.4, we used the following SN parameters: age $t = 17000$ yr, energy $E_0 = 5 \times 10^{50}$ erg, ejected mass $M_{\text{ej}} = 1.4 M_{\odot}$, ejecta power-law index $n = 0$ and CSM power-law index, $s = 0$. Density is given by the ISM density and is taken equal to 0.012 cm^{-3} . The package allows us to choose the ratio C/τ^* from the range 0, 1, 2 or 4. In this particular model, we selected the value of $C/\tau^* = 4$. Fig. 10 illustrates a screen capture of the results of this Leahy model considering a cloudy medium as proposed by WL. The results obtained by the code indicate that for the derived SNR age, the model reports a size of 26.29 pc, and a blast-wave

shock velocity of 581.2 km s^{-1} . These values are comparable with $R = 26$ pc and $V_s = 600 \text{ km s}^{-1}$ that we reported in this work. A significant difference in the electron temperature determination is found, as the code gave a value of 4.8×10^6 K, while with our observations a temperature $\sim 10^7$ K was determined. The simulated results can be compared with the values shown in Table 4 and we find that they agree.

To reproduce parameters such as temperature or emission measure, a standard model (Sedov–Taylor) is considered. In this case, the SN parameters such as SNR age, energy, ISM temperature and ejected mass were the same as the *Cloudy ISM* model, but the ejecta power-law index $n = 7$ and the ISM number density $n = 0.035 \text{ cm}^{-3}$ were taken into account to perform this model. Figure 11 illustrates the screen capture of the result of emission measure versus time.

8 DISCUSSION AND CONCLUSIONS

In the present work, we conducted a detailed study of SNR 0520–69.4 in the LMC based on *XMM–Newton* data. We have generated X-ray images and spectra of this object and find that the SNR shows a central bright X-ray morphology due to thermal emission (see Fig. 5 and the spectral fit presented in Section 4). Similar features were found in the SNRs W44 (Jones, Smith & Angelini 1993), 3C 391 (Rho & Petre 1996) and G272–3.2 (Harrus et al. 2001). Consequently, all of these are excluded from the group of SNRs whose centres are dominated by non-thermal emission, presumably due to a central pulsar.

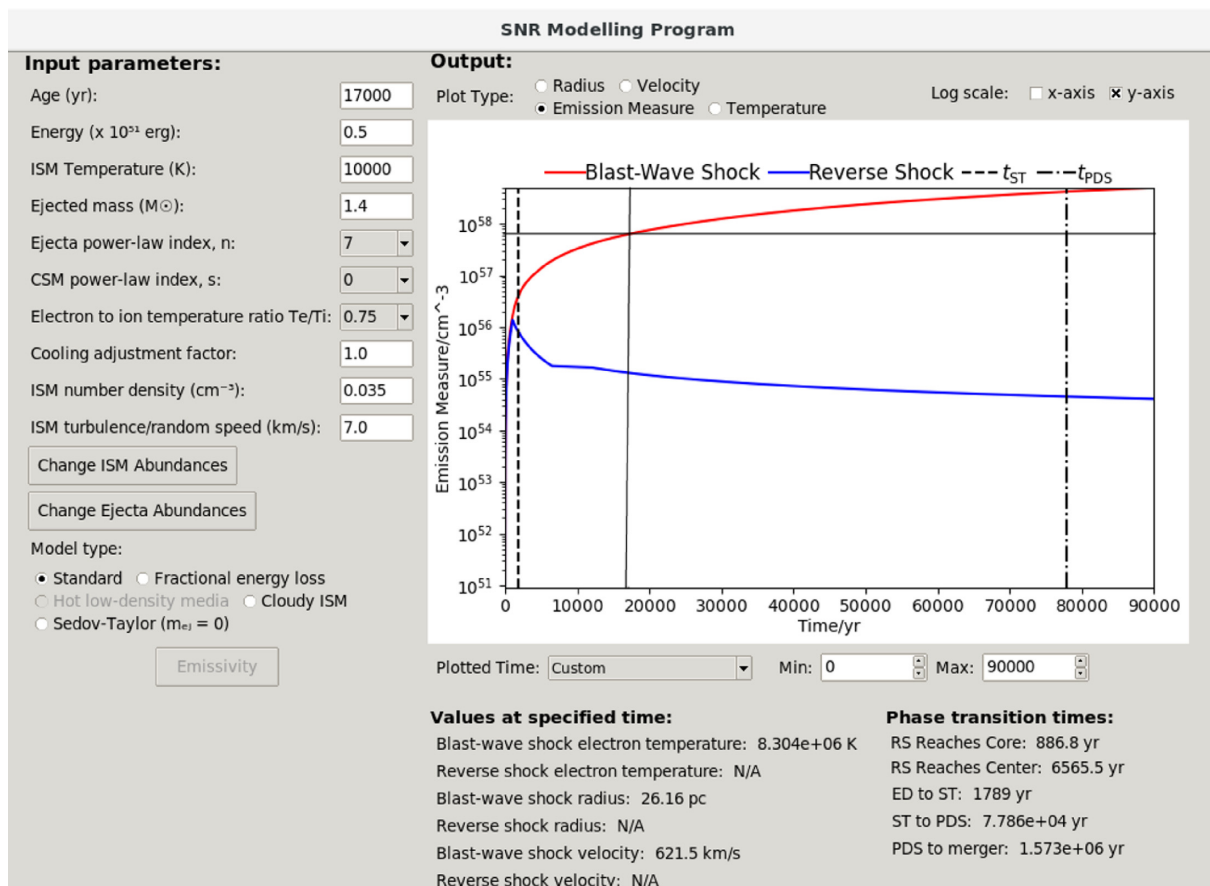


Figure 11. Screenshot of the main screen of the SNR modelling program. The boxes at the left side represent the input parameters. Top right: selection of the output plot of emission measure versus time; this plot represents the behaviour of the emission measure along the time corresponding to the blast-wave shock (red) and reverse shock (blue). Bottom right: output values at the specified time and the phase transition times. The vertical continuous line denotes the SNR age and the horizontal continuous line denotes respective emission measure.

From Fig. 6, we note that both X-ray and radio emissions have the same extensions. The different radial distributions of X-ray and radio intensities lead us to consider SNR 0520–69.4 as belonging to the category of MM SNRs.

In addition, from Figs 5 and 6, we see hot gas outside the radio emission boundary. In particular, we see X-ray emission through the north and south-east regions of the SNR. This suggests that there is leaking warm gas from the interior cavity to the outside of the optical and radio shell. However, when comparing the pressure in the optical with the pressure in X-ray, it can be seen that the value in the optical is \sim about one order of magnitude smaller than that in X-ray, which is expected as the hot gas inside the SNR shell is hotter than the gas emitting at the $H\alpha$ wavelength.

The WL model was put forward in an attempt to explain the MM class of SNRs as being caused by the evaporation of dense clouds that are overrun by the blast wave. From the optical observations at $H\alpha$, we estimate a cloud density ranging from 2.0 cm^{-3} to 2.6 cm^{-3} and taking the electron density derived from X-ray observations, 0.13 cm^{-3} as the intercloud density, we derive a C parameter that ranges from 15 to 20. In Table 4, we present the values for the parameters C and τ^* , and their ratio. Using the data from table 3 of WL, it was possible to obtain the value of the emission weighted temperature $\langle T \rangle$. Taking into account the tables published by WL for values of their parameters $C/\tau^* = 10$ as derived from Table 4 of the present work, we see that WL’s values are plausible regarding the values of the different parameters we

obtain. Furthermore, when comparing with the numerical model of Leahy & Williams (2017), we are able to obtain reasonable values for the parameters required in WL with the constrained values of radius and age obtained from the observations we analysed.

More observational studies and detailed modelling employing numerical simulations are needed to determine the origin and evolution of MM SNRs such as the one studied in this paper.

ACKNOWLEDGEMENTS

JR-I acknowledges financial support from TNM-SEP, DGAPA-PAPIIT (UNAM) grant IG100516. MR is grateful for financial support from DGAPA-PAPIIT (UNAM) IN109919 and CONACYT CY-253085 grants. We acknowledge the anonymous referee for useful comments that improved the paper, Dr Fabio de Colle for improving the English, and Dr Etienne Le Coarer.

DATA AVAILABILITY

The X-ray data underlying this article are available in *XMM–Newton Science Archive Search* at <http://nxsas.esac.esa.int/nxsas-web/#search> with the name of the object SNR 0520–69.4 and Obs. ID 0204770101, PI: K. Borkowski, (ODF files). Optical data were taken from the $H\alpha$ survey of the LMC (Ambrocio-Cruz et al. 2016).

REFERENCES

- Ambrocio-Cruz P., 1999, *Journal des Astronomes Francais*, 60, 35
- Ambrocio-Cruz P., Rosado M., Laval A., Le Coarer E., Russeil D., Amram P., 2008, *Rev. Mex. Astron. Astrofis.*, 44, 355
- Ambrocio-Cruz P. et al., 2016, *MNRAS*, 457, 2048
- Amram P., Boulesteix J., Georgelin Y. M., Georgelin Y. P., Laval A., Le Coarer E., Marcelin M., Rosado M., 1991, *The Messenger*, 64, 44
- Arnaud K. A., 1996, *Astronomical Data Analysis Software and Systems V*, 101, 17
- Chu Y.-H., Kennicutt R. C. Jr., 1988, *AJ*, 96, 1874
- Cox D. P., Anderson P. R., 1982, *ApJ*, 253, 268
- Crawford E. J., Filipovic M. D., Payne J. L., 2008, *Serbian Astronomical Journal*, 176, 59
- Dickey J. M., Lockman F. J., 1990, *ARA&A*, 28, 215
- Harris I. M., Slane P. O., Smith R. K., Hughes J. P., 2001, *ApJ*, 552, 614
- Jones L. R., Smith A., Angelini L., 1993, *MNRAS*, 265, 631
- Koyama K., Petre R., Gotthelf E. V., Hwang U., Matsuura M., Ozaki M., Holt S. S., 1995, *Nature*, 378, 255
- Kuntz K. D., Snowden S. L., 2008, *A&A*, 478, 575
- Le Coarer E., Amram P., Boulesteix J., Georgelin Y. M., Georgelin Y. P., Marcelin M., Joulie P., Urios J., 1992, *A&A*, 257, 389
- Le Coarer E., Rosado M., Georgelin Y., Viale A., Goldes G., 1993, *A&A*, 280, 365
- Leahy D. A., Williams J. E., 2017, *AJ*, 153, 239
- McKee C. F., Cowie L. L., 1975, *ApJ*, 195, 715
- Maggi P. et al., 2016, *A&A*, 585, A162
- Mathewson D. S., Ford V. L., Dopita M. A., Tuohy I. R., Long K. S., Helfand D. J., 1983, *ApJS*, 51, 345
- Osterbrock D. E., 1989, *Astrophysics of Gaseous Nebulae and Active Galactic Nuclei*. University Science Books, Mill Valley, CA
- Payne J. L., White G. L., Filipović M. D., 2008, *MNRAS*, 383, 1175
- Pietrzyński G. et al., 2013, *Nature*, 495, 76
- Rho J., Petre R., 1998, *ApJ*, 503, L167
- Rho J.-H., Petre R., 1996, *ApJ*, 467, 698
- Riess A. G. et al., 1998, *AJ*, 116, 1009
- Shannon C. E., 1949, *IEEE Proc.*, 37, 10
- Slane P., Hughes J. P., Edgar R. J., Plucinsky P. P., 1999, *Bulletin of the American Astronomical Society*, 31, 1418
- Smith R. C., Points S. D., Chu Y.-H., Winkler P. F., Aguilera C., Leiton R., 2005, *Bulletin of the American Astronomical Society*, 37, 1200
- Snowden S. L., Collier M. R., Kuntz K. D., 2004, *ApJ*, 610, 1182
- Snowden S. L., Mushotzky R. F., Kuntz K. D., Davis D. S., 2008, *A&A*, 478, 615
- Weaver R., McCray R., Castor J., Shapiro P., Moore R., 1977, *ApJ*, 218, 377
- White R. L., Long K. S., 1991, *ApJ*, 373, 543 (WL)
- Wilms J., Allen A., McCray R., 2000, *ApJ*, 542, 914

This paper has been typeset from a \LaTeX file prepared by the author.